Int. J. Solids Structures Vol 16, pp. 847–862
Pergamon Press Ltd., 1980 Printed in Great Britain

EFFECT OF GRAIN BOUNDARY SLIDING ON STEADY CREEP OF POLYCRYSTALS

F. GHAHREMANI

Division of Applied Sciences, Harvard University, Cambridge, MA 02138, U.S.A.

(*Received* 26 *April* 1979)

Abstract—The effect of grain boundary sliding on steady state creep of polycrystalline metals is analyzed by modeling the grain structure by an infinite two-dimensional array of regular hexagons in plane strain. A pure power-law relation is assigned to the grains and a Newtonian viscosity to the grain boundaries. The finite element method is used to approximately solve the resulting nonlinear boundary value problem. In this way, the overall stress–strain rate relation of the polycrystal is determined, and the contribution to total strain rate due to grain boundary sliding is calculated for various values of the hardening exponent. The results are compared with those of all other existing models.

1. INTRODUCTION

Numerous experiments on polycrystalline metals have convincingly demonstrated that at sufficiently high temperatures or at sufficiently low rates of deformation, resistance to slipping across the grain boundaries is low compared to resistance to plastic deformation in the interior of the grains[1–4]. Of great importance to engineering materials is the contribution of grain boundary sliding to total strain rate during steady creep of polycrystalline metals at high temperatures. We consider the range in which creep strains are of the order of 10^{-2}; that is, they are large compared to elastic strains (typically of the order of 10^{-4}), but yet they and their time derivatives are sufficiently small so that the small strain theory can be used. In this regime a pure power-law relation between strain-rate, ϵ, and stress is often found to characterize the behavior of metals quite well. On a $\log \epsilon$ vs $\log \sigma$ plot the power-law relation should give a straight line. However, a frequently observed characteristic feature of these plots is that they have an S-shaped portion[2–4], as shown schematically in Fig. 1. This phenomenon can be explained in terms of grain boundary sliding as follows. Assume that the material inside the grains satisfies the power-law relationship

$$\frac{\epsilon}{\epsilon_0} = \left(\frac{\sigma}{\sigma_0}\right)^n \tag{1}$$

where n is the hardening exponent of the material and σ_0 and ϵ_0 are constants. At very low strain rates the resistance to deformation of the grain boundaries is low compared to that of

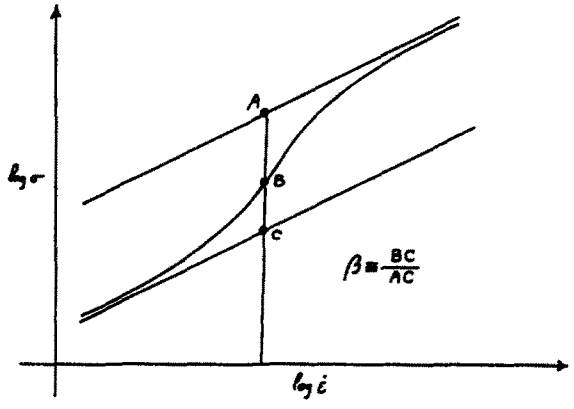

Fig. 1. Schematic illustration of the transition region.

grains. The grain boundaries therefore appear essentially as flaws in the material. The polycrystal obeys the relation

$$\frac{\epsilon}{\epsilon_0} = \left(f\frac{\sigma}{\sigma_0}\right)^n \quad (f > 1) \tag{2}$$

where f is called the stress enhancement factor. As the strain rate is increased, the resistance to deformation of grain boundaries increases faster than that of the grain material, until finally the grain boundaries become too strong to permit any appreciable sliding and transition is made from (2) to (1). The S-shaped portion of the curve in Fig. 1 is the transition region. Direct observations of the metallographically prepared surfaces of metals show increasing grain boundary offsets with decreasing strain rates in the transition region[2, 3].

In this paper the grain structure will be modeled by a two-dimensional array of regular hexagons in plane strain as shown in Fig. 2. We assume that the material inside the grains flows in accordance with the power-law relation (1) appropriately generalized to multi-axial states of stress. A Newtonian viscous relation will be assigned to the grain boundaries. The normal component of the velocity vector must be continuous across the boundaries, whereas its tangential component may suffer a jump proportional to the shearing traction on the boundary. The elastic strains will be neglected altogether. The overall applied stress will be taken to be a uniform tensile stress in the x-direction of Fig. 2. As a result of sliding the local stresses will be nonuniform. This model will be used to calculate the stress enhancement factor and the percentage of elongation rate due to grain boundary sliding and also to determine the shape and the position of the transition region.

2. FORMULATION OF THE PROBLEM

Consider the trapezoidal region $OIPQ$ in Fig. 2, henceforth referred to as the region A. If the state of stress in region A is known, by symmetry it is also known everywhere in the entire array. Therefore, provided one is able to derive the boundary conditions for region A and solve the resulting boundary value problem, then the local stresses and strain rates are everywhere known.

The boundary conditions, which are derived by using symmetry arguments, must be consistent with an overall applied stress in the x-direction. Let $\mathbf{U}(x, y) = U(x, y)\mathbf{i} + V(x, y)\mathbf{j}$ denote the velocity vector. Referring to Fig. 2, assume at the origin, point 0, $U = V = 0$ and at the point 0′, $U = u$ and $V = v$. The complete boundary conditions on OI, OQ, and IP are

$$\begin{cases} U = 0 & \tau_{xy} = 0 \quad \text{on } OI \\ V = 0 & \tau_{xy} = 0 \quad \text{on } OQ \\ V = v & \tau_{xy} = 0 \quad \text{on } IP. \end{cases} \tag{3}$$

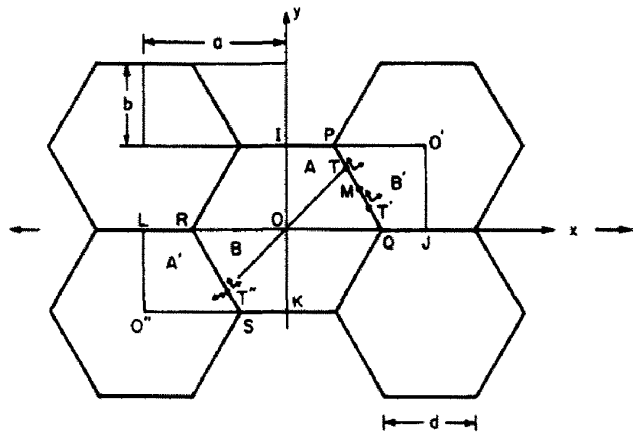

Fig. 2. Two-dimensional array of regular hexagons.

On PQ in the normal direction one has (for details see [11, 12])

$$\begin{cases} U_n(x, y) + U_n(a-x, b-y) = u_n & \text{on } PQ \quad (4a) \\ \sigma_n(x, y) = \sigma_n(a-x, b-y) & \quad (4b) \end{cases}$$

where U_n and $u_n(=\sqrt{3}\,u/2 + v/2)$ are the normal components of U and $\mathbf{u}(= u\mathbf{i} + v\mathbf{j})$; a and b are the length and the width of rectangle $OIO'J$. Equation (4a) expresses the requirement of continuity of normal velocity across the boundary. It is a relation between the normal component of the velocity vector at points $T:(x, y)$ and $T':(a-x, b-y)$ on the boundary. These two points are equidistant from M, where $M:(a/2, b/2)$ is the midpoint of the segment PQ in Fig. 2. Equation (4b) states that at points equidistant from M, the normal traction must be the same.

The tangential boundary condition on PQ is

$$\sigma_t = \frac{\eta}{w}[U_t] \tag{5}$$

where w is the thickness of the grain boundary, η the viscosity of the grain boundary material, and $[U_t]$ is the jump in the tangential component of velocity given by

$$[U_t] = u_t - U_t(a-x, b-y) - U_t(x, y) \tag{6}$$

with $u_t = -u/2 + \sqrt{3}\,v/2$, the tangential component of $\mathbf{u}$. The boundary conditions for region A are now complete; they are shown in Fig. 3.

We now formulate the boundary value problem in a convenient non-dimensional form. The governing equations are

$$\begin{cases} \sigma_{\alpha\beta,\beta} = 0 \qquad (\alpha, \beta = 1, 2) & (7a) \\ S_{\alpha\beta} = \dfrac{2}{3}\left(\dfrac{\epsilon_e}{\epsilon_0}\right)^{(1-n)/n} \dfrac{\sigma_0}{\epsilon_0}\,\epsilon_{\alpha\beta} & (7b) \\ \epsilon_{\alpha\beta} = \dfrac{1}{2}\left(\dfrac{\partial U_\alpha}{\partial x_\beta} + \dfrac{\partial U_\beta}{\partial x_\alpha}\right). & (7c) \end{cases}$$

The first is the equilibrium equation. The second is the stress–strain rate relation obtained by generalizing eqn (1) to multiaxial states of stress, where S is the stress deviation tensor and ϵ_e is the effective strain rate which in plane strain is given by

$$\epsilon_e = \sqrt{\frac{2}{3}\left(\epsilon_x^2 + \epsilon_y^2 + \frac{1}{2}\gamma_{xy}^2\right)}. \tag{8}$$

Introduce the notation

$$\begin{cases} \gamma_0 = \epsilon_0\left(\dfrac{\eta D \epsilon_0}{w\sigma_0}\right)^{n/1-n} \\ \tau_0 = \sigma_0\left(\dfrac{\eta D \epsilon_0}{w\sigma_0}\right)^{1/1-n} \end{cases} \tag{9}$$

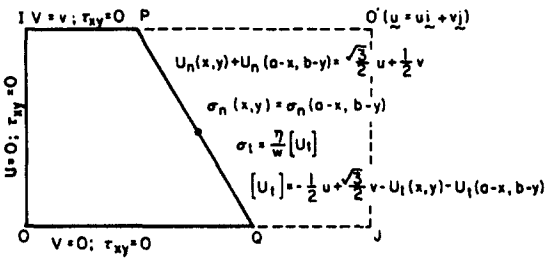

Fig. 3. Boundary conditions.

where we define the grain diameter D to be

$$D = \frac{4}{3} a \sqrt{\frac{3\sqrt{3}}{2\pi}} \tag{10}$$

i.e. the diameter of a circle whose area is the same as that of a hexagon. Then it can be shown that with

$$\hat{U}_\alpha = \frac{U_\alpha}{D\gamma_0}$$

$$\hat{\epsilon}_{\alpha\beta} = \frac{\epsilon_{\alpha\beta}}{\gamma_0} \tag{11}$$

$$\hat{\sigma}_{\alpha\beta} = \frac{\sigma_{\alpha\beta}}{\tau_0}$$

the governing nondimensional equations become

$$\begin{cases} \hat{\sigma}_{\alpha\beta,\beta} = 0 \left[(\,)_{,\alpha} = \dfrac{\partial(\,)}{\partial \hat{x}_\alpha}, \hat{x}_\alpha = \dfrac{x_\alpha}{D} \right] & \text{(12a)} \\ \hat{S}_{\alpha\beta} = \dfrac{2}{3} (\hat{\epsilon}_e)^{1-n/n} \hat{\epsilon}_{\alpha\beta} & \text{(12b)} \\ \epsilon_{\alpha\beta} = \dfrac{1}{2} (\hat{U}_{\alpha,\beta} + \hat{U}_{\beta,\alpha}) & \text{(12c)} \end{cases}$$

and with the exception of the eqn (5), every boundary condition in Fig. 3 remains the same provided a hat is placed over every quantity. Equation (5) becomes

$$\hat{\sigma}_t = [\hat{U}_t]. \tag{13}$$

In other words, the solutions of the boundary value problem for various values of the parameters (η, D, w, σ_0 and ϵ_0) are "similar." Therefore, if the quantities are normalized as in (11), the results will be valid universally for every material.

3. MACROSCOPIC RELATIONS

Although the microscopic boundary value problem is posed for region A, the macroscopic stresses and strain rates must be calculated by considering the complete rectangle $OIO'J$; see Fig. 2. In the boundary conditions (3)–(6), $\mathbf{u} = u\mathbf{i} + v\mathbf{j}$ is the velocity of the point O' relative to O. We assign an arbitrary value to v; then u is known from the condition of incompressibility of the material. This condition can be written as

$$\int_\Gamma U_i n_i \, dS = 0 \tag{14}$$

where Γ is any closed contour in the xy-plane and $\mathbf{n}$ its unit outward normal. For the rectangular region $OIO'J$ this equation gives

$$u = -\frac{a}{b} v. \tag{15}$$

The overall strain rates are given by

$$\bar{\epsilon}_x = \frac{u}{a}; \quad \bar{\epsilon}_y = \frac{v}{b}. \tag{16}$$

The overall stresses are calculated using

$$\begin{cases} \bar{\sigma}_x = \dfrac{1}{b}\displaystyle\int_{OI} \sigma_x \, \mathrm{d}y \\ \bar{\sigma}_y = \dfrac{1}{a}\displaystyle\int_{IP} \sigma_y \, \mathrm{d}x + \dfrac{1}{a}\int_{OQ} \sigma_y \, \mathrm{d}x. \end{cases} \tag{17}$$

The maximum overall shearing stress, which acts on the plane that bisects the angle between the x and the y axes, is

$$\bar{\tau} = \frac{\bar{\sigma}_x - \bar{\sigma}_y}{2}. \tag{18}$$

The maximum overall shearing strain is

$$\bar{\gamma} = \bar{\epsilon}_x - \bar{\epsilon}_y. \tag{19}$$

It is obvious that the plane strain configuration of hexagonal grains shown in Fig. 2, has a sixth order axis of symmetry. When grains are linear, $n = 1$, since a linearly elastic material with a sixth order axis of symmetry is transversely isotropic[13], the direction of the overall applied stress is immaterial. For nonlinear grains the material is not necessarily transversely isotropic and therefore the direction in which the overall stress is applied does matter. In anisotropic materials, the principal directions of the stress and strain rate tensors, in general, do not coincide. Nevertheless, from the boundary conditions (3)–(6) it follows that the principal directions of the overall stress and strain rate tensors defined above are the same; the x, y, and z-axes are themselves the principal directions for the class of deformations considered here.

The complete $\bar{\tau} - \bar{\gamma}$ relation can be written as

$$\frac{\bar{\tau}}{\tau_0} = \frac{1}{g}\left(\frac{1}{3}\right)^{n+1/2n}\left(\frac{\bar{\gamma}}{\gamma_0}\right)^{1/n}. \tag{20}$$

With τ_0 and γ_0 defined by (9), eqn (20) is valid universally for every material. In the above equation g, a function of $\bar{\gamma}$, is the stress enhancement factor. At very high strain rates, $\bar{\gamma} \to \infty$, very little sliding occurs, $g \sim 1$ and (20) approaches the stress–strain rate relation for the grains, i.e. (12b). At very low strain rates, $\bar{\gamma} \to 0$, g asymptotically approaches f, i.e. the stress enhancement factor for free sliding. Although the overall response of the material is in general anisotropic, the $\bar{\tau} - \bar{\gamma}$ relation is defined without ambiguity.

4. FINITE ELEMENT DISCRETIZATION

Nonlinearity and incompressibility of the material make the application of the finite element method difficult. In recent years several authors have discussed the problem of incompressibility[6–8]. In the method used here, which is developed by Needleman and Shih[6], the incompressibility constraint is imposed on the admissible displacement field by direct elimination of nodal displacements, and the nonlinear stiffness equation is solved by using the Newton-Raphson scheme. A brief description is given in Appendix A. Since boundary conditions are very uncommon, Needleman and Shih's method must be modified substantially; the complete details of these modifications are also given in Appendix A. The finite element grids are shown in Fig. 4.

5. NUMERICAL RESULTS

Figure 5(a) shows the plot of $\log(\bar{\tau}/\tau_0)$ vs $\log(\bar{\gamma}/\gamma_0)$ for $n = 2$ and the coarse grid. In this figure, since the transition region is relatively broad, the S-shape portion of the curve cannot be seen clearly. Alternatively, it is better to plot the parameter β, defined in Fig. 1, vs $\log(\bar{\gamma}/\gamma_0)$. Knowledge of f, β and n is completely sufficient for the determination of the $\log(\bar{\tau}/\tau_0) - \log(\bar{\gamma}/\gamma_0)$ relation. Figure 5(b) shows the plot of β vs $\log(\bar{\gamma}/\gamma_0)$ for $n = 2$ and the coarse grid.

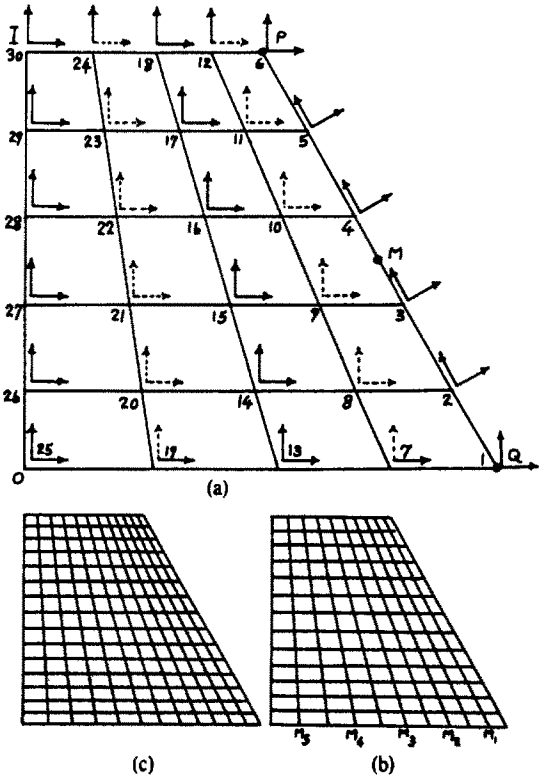

Fig. 4. Finite element grids, (a) coarse grid, (b) fine grid, (c) very fine grid.

This method of presenting the results is convenient also because the transition region for various values of n can be plotted on the same figure. Figure 6 shows the plot of β for $n = 2$ and $n = 4$ calculated using the fine grid. It can be seen that the width of the transition region decreases with respect to an increase in n.

Consider the rectangular region $OIO'J$ in Fig. 2. We define the fraction of elongation rate due to grain boundary sliding as

$$\frac{U_{GB}}{u} = \frac{-1}{2bu}\int_{OI}[U_t]\,dy \tag{21}$$

where $-[U_t]/2$ is the jump in the tangential component of velocity along PQ resolved in the x-direction. This definition is consistent with the experimental methods of grain boundary sliding in polycrystals[15, 16]. This formula also gives the fraction of strain rate due to grain boundary sliding. In the finite element solution $[U_t]$ is known only at the nodes on the boundary. The integral in (21) is calculated assuming $[U_t]$ to vary linearly between two successive nodes. Figure 7 shows the percentage elongation rate due to sliding vs $\log(\bar{\gamma}/\gamma_0)$ for $n = 4$.

Comparison with Hart's model

For simple shear, in our notation Hart's equations are[4]

$$\begin{cases} \dfrac{\bar{\tau}}{\tau_0} = \dfrac{1}{g}\left\{\dfrac{1}{3}\right\}^{(n+1)/2n}\left(\dfrac{\bar{\gamma}}{\gamma_0}\right)^{1/n} & (22) \\ g = \dfrac{f}{1+(f-1)z} & (23) \\ z^n + \left(\dfrac{\bar{\gamma}}{\gamma_T}\right)^{(1-n)/n} z - 1 & (24) \end{cases}$$

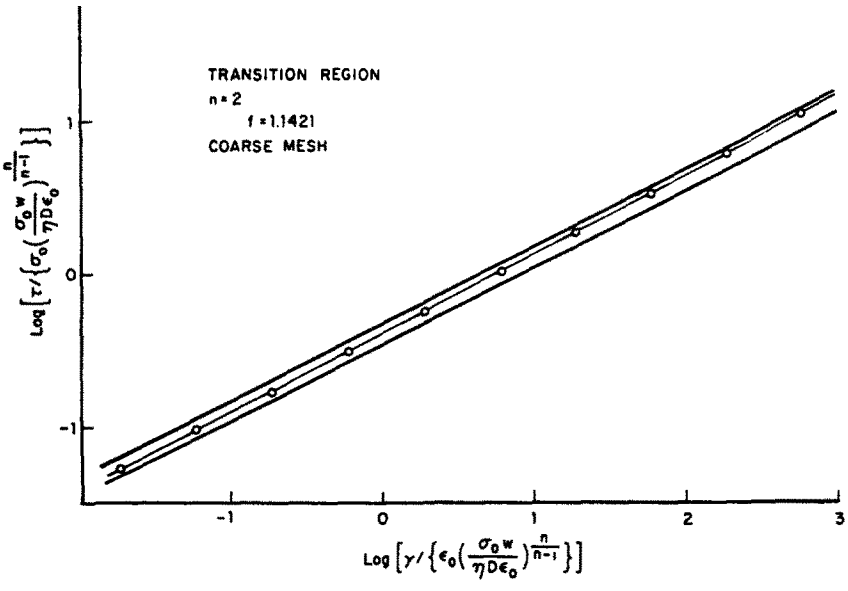

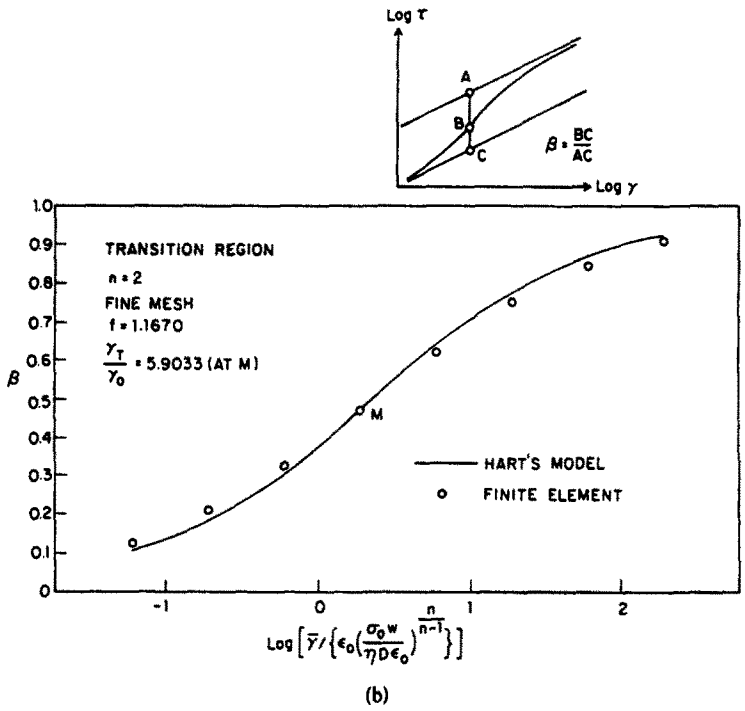

Fig. 5. Transition region for $n = 2$ coarse grid.

where f and γ_T are phenomenological constants. For given values of γ_T and f, at an overall strain rate $\bar{\gamma}$ one can calculate z by using (24), then from (23) g is known. Therefore, in addition to γ_0 and τ_0, specification of f and γ_T completely define the behavior of the material. The parameter z ranges from 0 to 1; for $z = 0$, $g = f$ and (22) is the equation for free sliding; for $z = 1$, $g = 1$ and (22) reduces to the equation for no sliding. Hart's model, which is similar to the spring-dashpot models for viscoelastic materials, predicts neither the magnitude of f nor the position of the transition; it merely reduces the problem to the determination of the parameters f and γ_T. We can compare Hart's results with ours only by assigning to f and γ_T values predicted by our finite element program and seeing whether the shape of the transition region is the same for the two models.

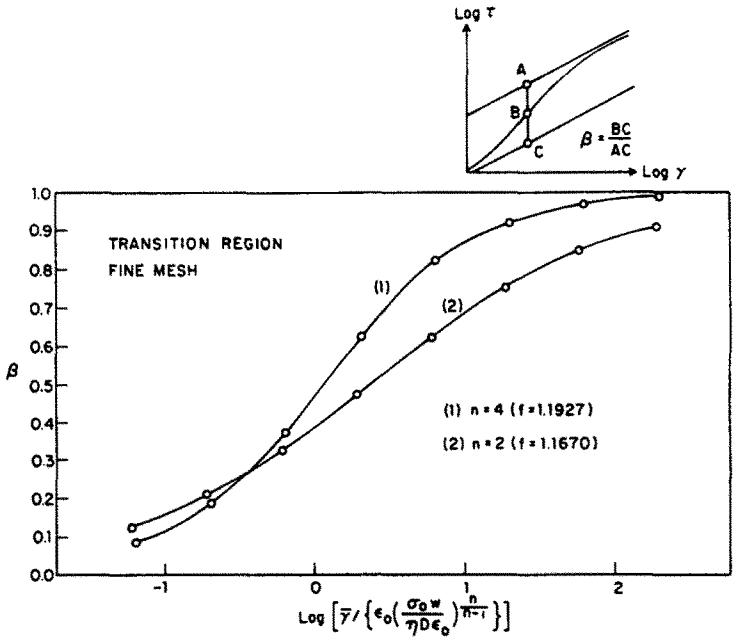

Fig. 6. Transition region for $n = 2$ and $n = 4$, fine grid.

Figure 8 shows the transition region for $n = 2$ as predicted by the Hart model (the solid line) and the finite element program (the circles). It can be seen that the agreement between the two theories is satisfactory. The phenomenological parameter γ_T was evaluated at the point M.

Free sliding

We now discuss the important limiting case of free sliding.† Dimensional analysis shows that f, the stress enhancement factor for free sliding, is a function of n only. Figure 5 shows plot of f vs $1/n$. Curves labeled (1) and (2) were obtained by using the fine and the coarse grids

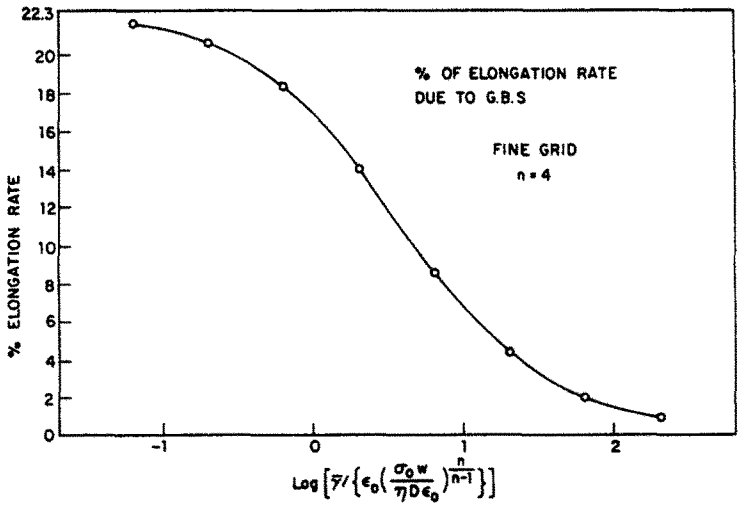

Fig. 7. Percentage elongation rate due to grain boundary sliding vs Log $(\bar{\gamma}/\gamma_0)$.

†It is more convenient to do these calculations by setting $\eta = 0$ rather than $\bar{\gamma} \to 0$. Then, on the boundary PQ in Fig. 2 $\sigma_t = 0$ and the overall equation is

$$\frac{\bar{\tau}}{\sigma_0} = \frac{1}{f}\left(\frac{1}{3}\right)^{n+1/2n}\left(\frac{\bar{\gamma}}{\epsilon_0}\right)^{1/n}$$

which is obtained from (2).

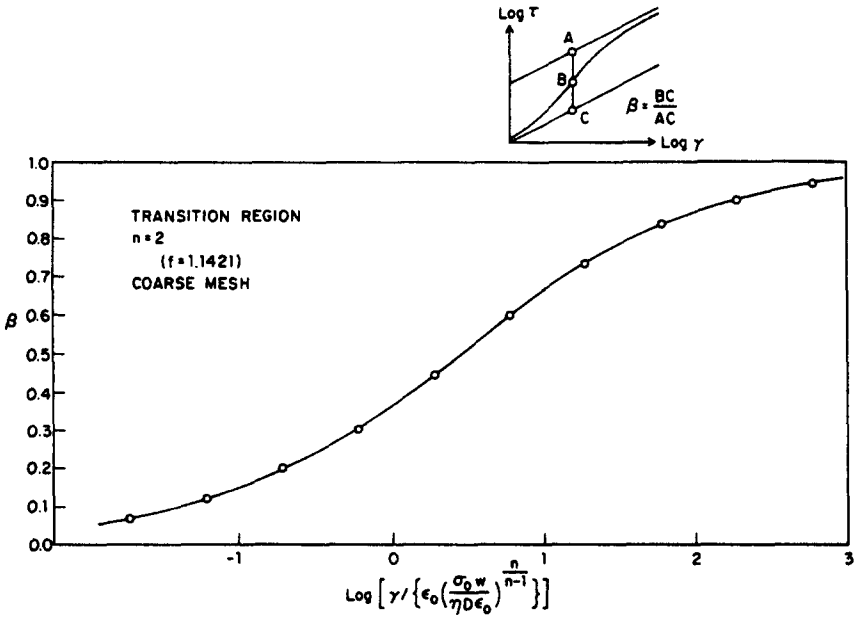

Fig. 8. Transition region, comparison with Hart's model.

shown respectively in Figs. 4(a) and 4(b). The point labeled (4) (for $n = 1$) is calculated using the very fine mesh shown in Fig. 4(c). It can be seen that the result converges very rapidly as the mesh is refined. The very fine grid is not used for calculations in the nonlinear range.

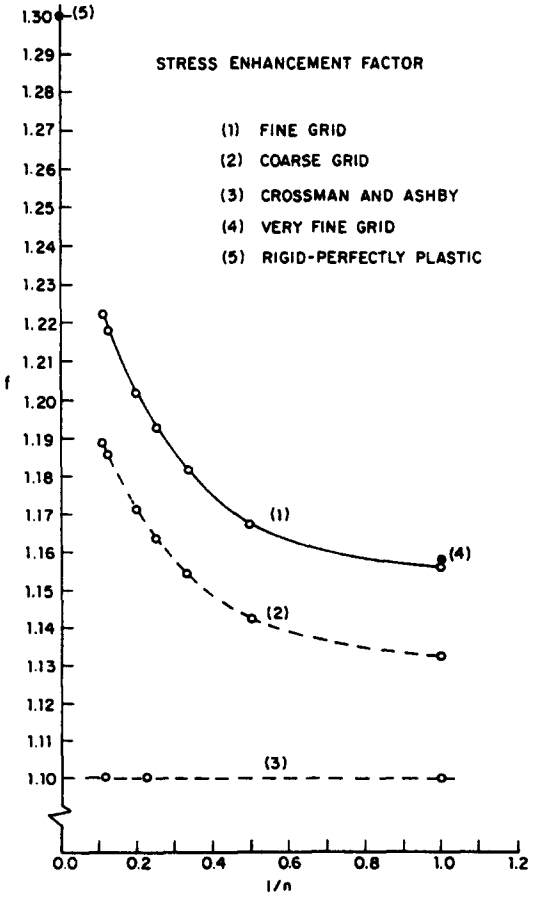

Fig. 9. Stress enhancement factor vs $1/n$.

For the limiting case of rigid-perfectly plastic grains ($n = \infty$), Chen and Argon[14] have estimated f from slip line theory to be 1.3. This is the point labeled (5) in Fig. 9. Curve (1) appears to approach this point as n increases ($1/n \to 0$).

For values of n of 1.0, 4.4 and 8.8, Crossman and Ashby[5] found that f was 1.1 ± 0.01. The straight line labeled (3) is a plot of their results. They did their calculations for simple shear along the x-axis of Fig. 2. However, because of the overall transverse isotropy in the linear range, their results must coincide with ours for $n = 1$. This discrepancy may be explained as follows. Firstly, since Crossman and Ashby have not at all mentioned the numerical difficulties associated with material incompressibility, their steady state limiting results may be inaccurate. Secondly, in Fig. 2 instead of applying the jump conditions of the type (5) along PQ, which represents a grain boundary, Crossman and Ashby gave the grain boundary a finite thickness (approximately $D/130$) and modeled it by elements. (They used constant strain triangles in all of their calculations.) This assumed thickness, which is much larger than the actual width of the grain boundaries, was introduced only for ease of computation. But since elements in this narrow boundary region must be connected to the elements in the interior at the nodes on the interface, it follows that their aspect ratios must have been disproportionately larger than those of the elements inside the grains. This procedure not only led to the inaccuracy of the computations, it also forced them to restrict themselves to a relatively coarse finite element mesh. Thirdly, for $n = \infty$ ($1/n = 0$) and simple shear along the x-axis, f has been estimated by Crossman and Ashby[7] to be 1.5. Apparently the straight line in Fig. 9 does not approach 1.5 as n increases.

For $n = 1$ the reciprocal of f gives $\bar{G}/G$, i.e. the ratio of the relaxed to the unrelaxed shear modulus. In [11, 12] we calculated $\bar{G}/G$ as a function of Poisson's ratio ν for the hexagonal grains in Fig. 2. It was shown that as $\nu \to 1/2$ (i.e. the material becomes nearly incompressible), $\bar{G}/G$ approached $1/f$ as computed here. This is a check on the accuracy of the results, since the finite element program used to calculate $\bar{G}/G$ was entirely different from the one used to compute f here.

The percentage of elongation rate due to grain boundary sliding was defined by (21). For free sliding this is plotted in Fig. 10. For rigid-perfectly plastic grains, Brunner and Grant[15] estimated this percentage to be 33, which is represented as point (3) in Fig. 6.

Although at the triple point P in Fig. 2 the stresses and the strain rates are singular, the finite element approximation, which gives only the average stress in an element, does not reveal the character of this singularity; it yields stresses and strain rates that are finite in every element. The maximum stress occurs in the element located at the corner P. Lau and Argon[17] have examined the stress and strain rate singularity at the triple grain junction caused by grain boundary sliding.

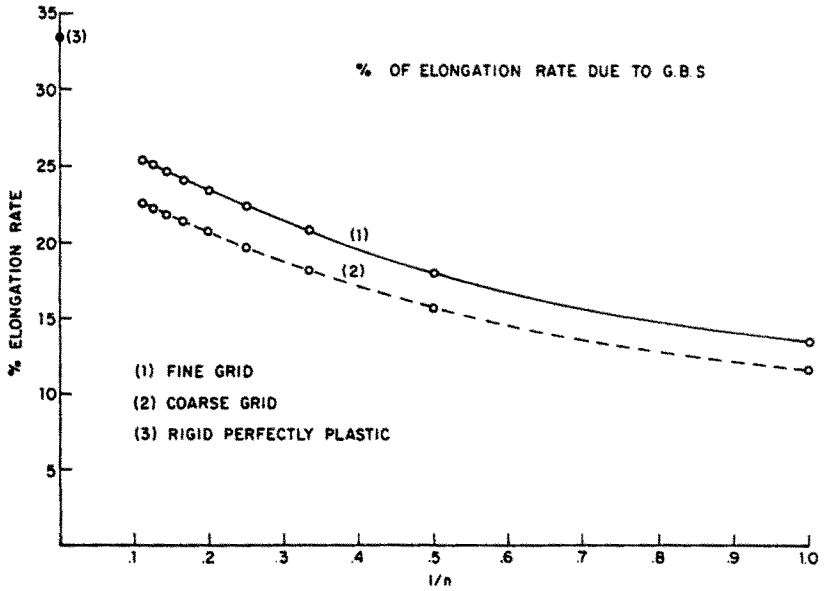

Fig. 10. Percentage elongation rate due to grain boundary sliding vs $1/n$.

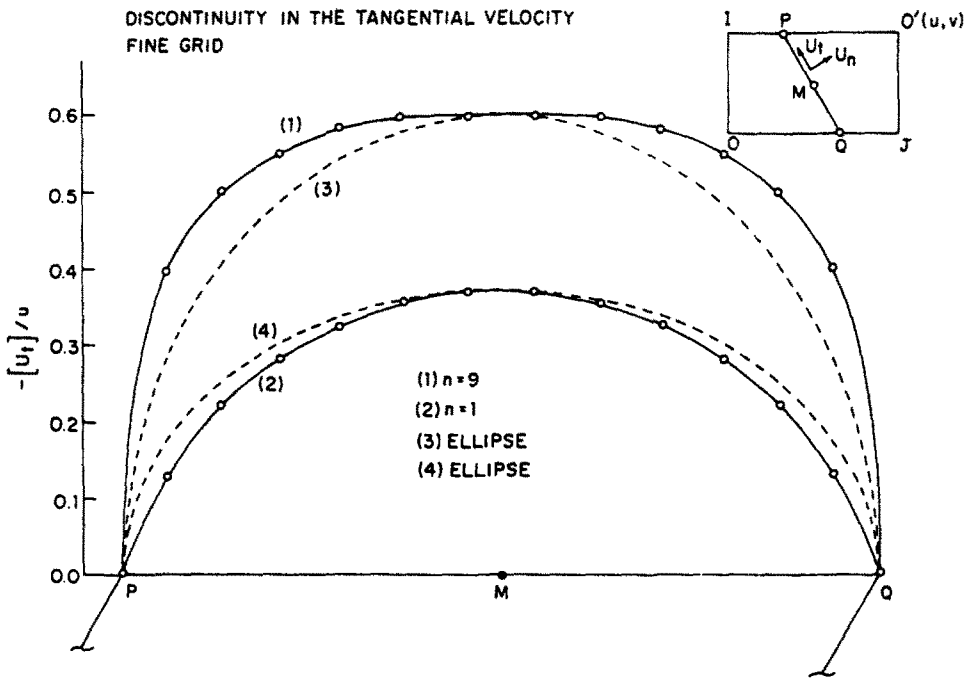

Fig. 11. Discontinuity in the tangential velocity.

It is of interest to study the distribution of the jump in the tangential velocity along the boundary PQ of Fig. 2. For the fine grid this is shown in Fig. 11. The solid lines labeled (1) and (2) correspond to $n = 9$ and $n = 1$, respectively. In the linear case, $n = 1$, using the very fine grid, we found that the result was indistinguishable from curve 2. For an isolated straight crack in a linearly elastic isotropic material, simple plane strain solutions indicate that the distribution of this jump along the crack is an ellipse (see, e.g. [15]). For comparison two ellipses with the same major and minor axes as the computed curves are drawn in Fig. 11.

In plane strain, for a rigid-perfectly plastic material the slip lines are defined as the two orthogonal families of curves whose directions at every point coincide with those of maximum shear strain rate [18]. When there is no sliding the slip lines for region A are shown in Fig. 12(a); they are simply straight lines at 45 degrees to the coordinate axes. For free sliding, finding the direction of maximum shear strain rate in every element and drawing two smooth orthogonal families of curves along them, we obtain the plot shown in Fig. 11(b). Since on the boundaries the shearing stress vanishes, these lines intersect every boundary, including PQ, at 45 degrees. Figure 11(b) is for $n = 9$; as n increases, this orthogonal net approaches the slip-lines, which are the characteristics of the hyperbolic system of equations that govern the limiting case of rigid-perfectly plastic material. Figure 11(c) shows these slip-lines obtained by Brunner and Grant [15].

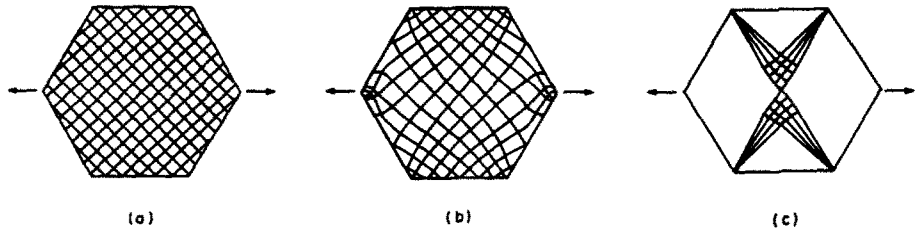

Fig. 12. Lines of maximum shear strain rate; (a) no sliding; (b) free sliding, $n = 9$; (c) free sliding $n = \infty$.

Acknowledgement—The author wishes to express his deepest gratitude to Professor Hutchinson for suggesting the problem and for his guidance and to Professors Budiansky and Sanders for their assistance. Thanks are also due to Professor A. Needleman of the Division of Engineering, Brown University for making available his computer program and his generous assistance. This work was supported in part by the National Science Foundation under Grants NSF-ENG78-10756 and NSF-DMR77-24295, and by the Division of Applied Sciences, Harvard University.

REFERENCES

1. C. Zener, *Elasticity and Anelasticity of Metals*. The University of Chicago Press, Chicago (1948).
2. H. E. Cline and T. H. Alden, Rate-sensitive deformation in tin-lead alloys. *Trans. AIME* **239**, 710 (1967).
3. G. L. Wire, H. Yamada and Che-Yu Li, Mechanical equation of state and grain boundary sliding in lead in monotonic loading. *Acta Met.* **22**, 505 (1974).
4. E. W. Hart, A theory of flow of polycrystals. *Acta Met.* **15**, 1545 (1967).
5. F. W. Crossman and M. F. Ashby, The non-uniform flow of polycrystals by grain boundary sliding accommodated by power-law creep. *Acta Met.* **23**, 425 (1975).
6. A. Needleman and C. F. Shih, A Finite element method for plane strain deformation of incompressible solids. *Comp. Meth. Appl. Mech. Eng.* **15**, 223 (1978).
7. N. L. Goldman and J. W. Hutchinson, Fully plastic crack problems: the center-cracked strip under plane strain. *Int. J. Solids Structures* **11**, 575 (1975).
8. J. C. Nagtegaal, D. M. Parks and J. R. Rice, On numerically accurate finite element solutions in fully plastic range. *Comp. Meth. Appl. Mech. Eng.* **4**, 153 (1974).
9. C. S. Desai and J. F. Abel, *Introduction to the Finite Element Method*. Van Nostrand Reinhold, New York (1972).
10. O. C. Zienkiewicz, *The Finite Element Method*, 3rd Edn. McGraw-Hill, New York (1977).
11. F. Ghahremani, An Analysis of Grain Boundary Sliding, Ph.D. Thesis, Harvard University (1978).
12. F. Ghahremani, Effect of grain boundary sliding on anelasticity of polycrystals. *Int. J. Solids Structures*. **16**, 825–845 (1980).
13. S. G. Lekhnitski, *Theory of Elasticity of an Anisotropic Elastic Body*, Holden-Day, San Francisco (1963).
14. I. W. Chen and A. S. Argon, Steady state power-law creep in heterogeneous alloys with and without grain boundary sliding. To appear in *Acta Met.*
15. H. Brunner and N. J. Grant, Deformation resulting from boundary sliding. *Trans. AIME* **215**, 48 (1959).
16. R. C. Gifkins, The measurement of grain boundary sliding in polycrystalline specimens. *The Institute of Metals* **7**, 15 (1973).
17. C. W. Lau and A. S. Argon, Stress concentration caused by grain boundary sliding in metals undergoing power-law creep. *Proc. Int. Fracture Conference*. Waterloo, Canada (1977).
18. R. Hill, *The Mathematical Theory of Plasticity*, Clarendon Press, Oxford (1950).
19. C. F. Shih, J-integral estimates for strain hardening materials in antiplane shear using fully plastic solution. *Mechanics of Crack Growth*, ASTM, STP590, 3 (1976).
20. G. Dahlquist and A. Bjork, *Numerical Methods*. Prentice-Hall, New Jersey (1974).

APPENDIX A

Details of the finite element technique

In this appendix the Needleman-Shih finite element technique will be explained briefly. This explanation is sufficient to understand the changes that had to be made in order to apply their method to our problem.

As we shall discuss later in detail, the nonlinear stiffness equation will be solved by using the Newton-Raphson method. To isolate the difficulties, at first the method of incorporating the incompressibility constraints will be explained for a linear material; then the necessary steps for passing to the general case of nonlinear material behavior will be indicated. Therefore we now assume that the material is linear.

Because of the incompressibility, only a few element types and arrangements can be used. With arbitrary elements if the mesh is refined, the number of constraints imposed by incompressibility may increase faster than the number of degrees of freedom. Figure 13(a) shows a quadrilateral element composed of four constant strain triangles. Point M is the intersection of the diagonals AC and BD. This special arrangement has the property that if the incompressibility constraint is satisfied in three of the triangles, the constraint in the fourth triangle is automatically satisfied. It can be shown that with this element the number of degrees of freedom increases faster than the number of constraints as the mesh is refined [8].

Therefore, there are only three constraints (of the form $\epsilon_x + \epsilon_y = 0$) per quadrilateral element rather than four. Two of these can be used to eliminate the two degrees of freedom at the central node M in Fig. 13(a). The remaining constraint is used to combine quadrilateral elements to form a substructure as in Fig. 13(b). This particular substructure has 10 elements; consequently, 10 degrees of freedom on the central node can be eliminated. They are drawn by using dashed lines.

Let $\{q_s\}$ denote the vector of nodal velocities for the substructure; to be concrete, the reference is made to the typical substructure shown in Fig. 13(b). The equation of constraints is

$$[H]\{q_s\} = 0 \tag{A1}$$

where $[H]$ is a 10 (the number of constraints per substructure) by $3b$ (total number of degrees of freedom in the substructure) matrix. Let $\{q_s\}$ be partitioned as

$$\{q_s\} = \begin{Bmatrix} q_f \\ q_e \end{Bmatrix} \tag{A2}$$

where $\{q_e\}$ is the vector of eliminated velocities and $\{q_f\}$ is the vector of remaining (free) velocities. Using (A1), we solve for $\{q_e\}$ in terms of $\{q_f\}$ as

$$\{q_e\} = [G]\{q_f\} \tag{A3}$$

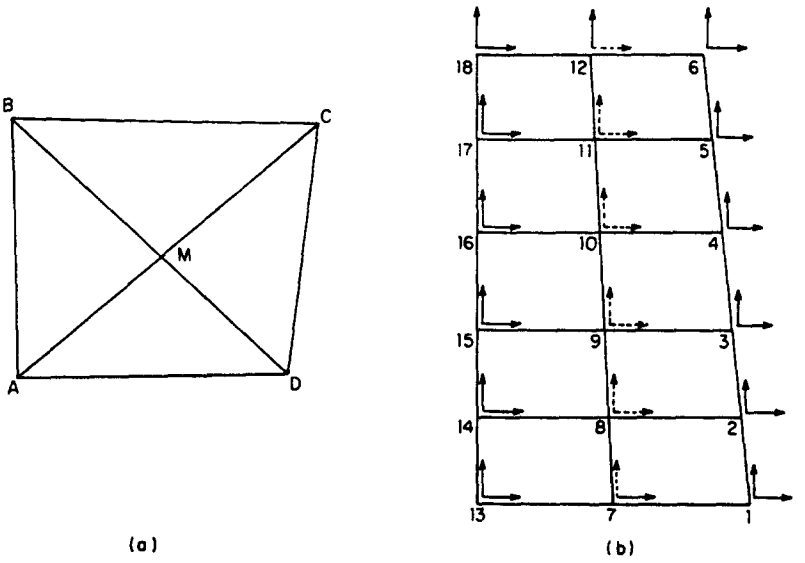

Fig. 13. (a) Quadrilateral element, (b) a substructure.

where $[G]$ is a 10 by 26 (the number of free degrees of freedom in the substructure) matrix. However, it is important to observe that, one is not free to arbitrarily eliminate any 10 degrees of freedom in the substructure; if $\{q_e\}$ is to be eliminated the 10×10 coefficient matrix of these displacement rates in the constraints (A1) must be nonsingular. These substructures are the basic building blocks of the finite element grid. A coarse mesh composed of two substructures is shown in Fig. 4(a).

By assembling the 8×8 stiffness matrices of the quadrilaterals, one obtains the stiffness matrix of a substructure, $[K_s]$. The principle of virtual work for the substructure is

$$\{\delta q\}^T[K_s]\{q_s\} = \{\delta q\}^T\{Q_s\} \tag{A4}$$

where $\{q_s\}$ and $\{Q_s\}$ are velocity and load vectors for the substructure and $\{\delta_q\}$ is the vector of virtual velocities. Partitioning this equation as in (A2), one obtains

$$\begin{Bmatrix}\delta q_f \\ \delta q_e\end{Bmatrix}\begin{bmatrix}K_{ff} & K_{fe} \\ K_{ef} & K_{ee}\end{bmatrix}\begin{Bmatrix}q_f \\ q_e\end{Bmatrix} = \begin{Bmatrix}\delta q_f \\ \delta q_e\end{Bmatrix}^T\begin{Bmatrix}Q_f \\ Q_e\end{Bmatrix}. \tag{A5}$$

But from (A3)

$$\{\delta q_e\} = [G]\{\delta q_f\}. \tag{A6}$$

Substitution of (A6) into (A5) gives

$$\{\delta q_f\}^T[K_s']\{q_f\} = \{\delta q_f\}^T\{Q_s'\} \tag{A7}$$

where

$$[K'] = [K_{ff}] + [K_{fe}][G] + [G]^T[K_{ef}] + [G]^T[K_{ee}][G] \tag{A8}$$

$$\{Q_s'\} = \{Q_f\} + [G]^T\{Q_e\}. \tag{A9}$$

Equations (A8) and (A9) give the modified stiffness matrix and load vector for the substructure after the elimination process. By assembling these, one obtains the master load vector $\{Q\}$ and stiffness matrix $[K]$ which is symmetric and positive definite. The equilibrium equation for the assemblage is

$$[K]\{q\} = \{Q\} \tag{A10}$$

where $\{q\}$ is the overall vector of free velocities.

The boundary conditions on OI and IP of Fig. 3 can be implemented easily by the usual methods. For example, for nodes on IP to apply $\tau_{xy} = 0$ we simply make the tangential component of the load vector on these nodes equal to zero. To implement $V = v$ for degree of freedom i say, $q_i = v$, we first modify the load vector according to

$$Q_j' = Q_j - K_{ji}v \quad \text{for} \quad i \neq j \quad \text{and} \quad Q_i' = v. \tag{A11}$$

Then the ith row and the ith column of the stiffness matrix are made zero and the diagonal element, K_{ii}, is made unity, according to standard procedures.

The implementation of the boundary conditions on OQ and PQ pose special difficulties. For definiteness we explain these by referring to the grid shown in Fig. 4(a). From the form of boundary conditions (see Fig. 3) it follows that nodes on PQ must be arranged in pairs of points equidistant from M. With the exception of nodes at P and Q, the degrees of freedom at other nodes on PQ must be referred to the normal and the tangential directions. Introduce the notation

$$\begin{cases} F_x(i),\ F_y(i) & \text{force in the } x \text{ and } y \text{ directions on node } i \\ F_n(i),\ F_t(i) & \text{force in the normal and tangential directions on node } i \\ U(i),\ V(i) & \text{displacements in the } x \text{ and } y \text{ directions on node } i \\ U_n(i),\ U_t(i) & \text{displacements in the normal and the tangential direction on node } i \\ q_1 = U(1),\ q_2 = V(1),\ q_3 = U_n(2),\ q_4 = U_t(2)\ldots \\ Q_1 = F_x(1),\ Q_2 = F_y(1),\ Q_3 = F_n(2),\ Q_4 = F_t(2)\ldots \end{cases} \tag{A12}$$

On PQ, from Figs. 3 and 4(a), the boundary conditions are

$$\begin{cases} U(1) + U(6) = u \\ U_n(2) + U_n(5) = \dfrac{\sqrt{3}}{2}u + \dfrac{1}{2}v \\ U_n(3) + U_n(4) = \dfrac{\sqrt{3}}{2}u + \dfrac{1}{2}v \\ F_t(2) = \dfrac{\eta}{w}\left\{\left(\dfrac{l_1}{3} + \dfrac{l_2}{3}\right)\left[\dfrac{-1}{2}u + \dfrac{\sqrt{3}}{2}v - U_t(2) - U_t(5)\right]\right. \\ \qquad \left. + \dfrac{l_2}{6}\left[\dfrac{-1}{2}u + \dfrac{\sqrt{3}}{2}v - U_t(3) - U_t(4)\right]\right\} \\ F_t(3) = \dfrac{\eta}{w}\left\{\dfrac{l_2}{6}\left[\dfrac{-1}{2}u + \dfrac{\sqrt{3}}{2}v - U_t(2) - U_t(5)\right]\right. \\ \qquad \left. + \left(\dfrac{l_2}{3} + \dfrac{l_3}{2}\right)\left[\dfrac{-1}{2}u + \dfrac{\sqrt{3}}{2}v - U_t(3) - U_t(4)\right]\right\} \end{cases} \tag{A13}$$

and

$$\begin{cases} F_x(1) = F_x(6) \\ F_n(2) = F_n(5) \\ F_n(3) = F_n(4) \\ F_t(2) = F_t(5) \\ F_t(3) = F_t(4). \end{cases} \tag{A14}$$

In obtaining the last two equations in (A13) we made use of the following result. Assuming that the shearing traction σ_t varies linearly between two successive nodes i and j on the boundary, the contribution to the tangential nodal forces due to the traction on the segment ij is [9]

$$\begin{cases} F_t(i) = l\left(\dfrac{\sigma_t(i)}{3} + \dfrac{\sigma_t(j)}{6}\right) \\ F_t(j) = l\left(\dfrac{\sigma_t(i)}{6} + \dfrac{\sigma_t(i)}{3}\right) \end{cases} \tag{A15}$$

where $\sigma_t(i)$ and $\sigma_t(j)$ are the values of σ_t at nodes i and j and l is the length of the segment ij.

Another difficulty in applying the boundary conditions arises on OQ in Fig. 3. Since boundary nodal degrees of freedom have been eliminated from the grid, the Needleman-Shih method is not applicable to arbitrary boundary conditions [6]. In Fig. 4(a), the vertical degrees of freedom at the nodes 7 and 19 have been eliminated. Although, one can easily assign $V(1) = V(13) = V(25) = 0$, obviously $V(7) = V(19) = 0$ cannot be prescribed. Therefore, it is necessary to extend the Needleman-Shih method to cover arbitrary velocity and traction boundary conditions.

Formula (A9) shows that the nodal forces at the eliminated degrees of freedom have been distributed on the nodal forces at the degrees of freedom that have not been eliminated. Therefore, although arbitrary velocity boundary conditions cannot be applied, it is possible to prescribe arbitrary surface tractions. We make use of this fact to satisfy the velocity boundary conditions on OQ of Fig. 4(a). The method is in essence as follows: two forces will be applied in the y-direction at the nodes 7 and 19 and adjusted so as to make the vertical velocities at these nodes vanish.

The boundary conditions for the velocities in Fig. 4(a) are such that the incompressibility eqn (14) is satisfied, in other words, there is no change in the area of region A after deformation. Therefore, if a vertical force is applied at the node 7 so as to make $V(7)$ vanish, $V(19)$ must vanish automatically, i.e. without having to apply a vertical force at the node 19 and vice versa. The two cases are, however, identical to within an overall hydrostatic state of stress. For the fine grid, consisting of five substructures shown in Fig. 4(b), it is necessary to apply four vertical forces at any four of the five nodes M_1, M_2, M_3, M_4 and M_5 to make the vertical velocities at these nodes zero; the vertical velocity at the fifth node must vanish automatically. In our calculations forces were applied at nodes M_1, M_2, M_3, and M_4 for the fine grid and at the node 7 for the coarse grid. At the remaining node the vertical velocity came out zero as a result of computation.

Using the coarse grid shown in Fig. 4(a), we now explain the numerical application of the boundary conditions on OQ and PQ. Consistent with (A13) introduce the notation

$$\begin{aligned}\lambda_1 &= F_x(1) = F_x(6)\\ \lambda_2 &= F_n(2) = F_n(5)\\ \lambda_3 &= F_n(3) = F_n(4)\\ \lambda_4 &= F_t(2) = F_t(5)\\ \lambda_5 &= F_t(3) = F_t(4).\end{aligned} \tag{A16}$$

Further, let

$$\mu_1 = F_y(7). \tag{A17}$$

In the final overall equilibrium equation, only the free velocities appear. Denote the vector of these velocities by $\{q\}$. Then one has

$$q_i = \sum_{k=1}^{5} a_{ik}\lambda_k + \sum_{k=1}^{1} b_{ik}\mu_k + q_i^0 \quad (i = 1, N) \tag{A18}$$

where N is the total number of free velocities. For the fine mesh, shown in Fig. 4(b), there are four μ's rather than one, and the matrix $[b_{ik}]$ is $N \times 4$.

To calculate q_i^0 in (A18) we set $\lambda_i = \mu_1 = 0$ $(i = 1, 5)$ and solve the resulting system (A10). The influence coefficients a_{ik} and b_{ik} can be calculated likewise by setting one of the λ_i $(i = 1, 5)$ and μ_1 equal to unity and the rest equal to zero and solving the system (A10). This procedure involves repeated solution of eqn (A10) for various load vectors $\{Q\}$. This can be done by first using Choleski's method to decompose the stiffness matrix as $[K] = [U]^T[U]$, where $[U]$ is an upper triangular matrix. Then, each time $\{Q\}$ is changed, it is only necessary to carry out the back and forward substitutions by using the same matrix $[U]$. The computer time required to decompose the stiffness matrix is by far more than that spent on back and forward substitutions. Therefore, this process increases the computation time only slightly.

Having found a_{ij}, b_{ij}, and q_i^0; eqns (A18) are substituted into (A13) to obtain five equations for λ_i $(i = 1, 5)$. To find an equation for μ_1, we consider the substructure containing the node 7 in Fig. 4(a). The eliminated velocities in this substructure are given in terms of the free velocities by an equation similar to (A3). In particular V(7) is given by

$$V(7) = \sum_{i=1}^{N} g_i^1 q_i$$

where g_i^1 $(i = 1, N)$ are certain known coefficients. Since $V(7) = 0$, the above equation gives

$$\sum_{i=1}^{N} g_i^1 q_i = 0. \tag{A19}$$

Substituting (A18) into (A19), one obtains the equation for μ_1. The complete system consisting of six equations for the six unknowns λ_i $(i = 1, 5)$ and μ_1, is very well conditioned. After solving this system, by (A18) the free velocities are known, and by equations of the type (A3) for each substructure, the eliminated velocities are calculated. For each triangular element, the strain rates are found by using the usual matrix relating the vector of nodal velocities to the strain rates in the element [10]. This strain rate tensor is deviatoric. The stress deviation tensor is calculated using the power law relation (7b). The hydrostatic stress, although not difficult to calculate [6], will not be computed since it will not be used afterwards.

In order to concentrate only on the problem of incompressibility, so far it has been assumed that the material is linear. Now the necessary steps for passing to the general case of nonlinear material behavior will be discussed. According to Newton-Raphson's method, the jth increment in the velocities, $\{\Delta q_j\}$, for a triangle is given by [6, 10].

$$A[B]^T[D_t][B]\{\Delta q_j\} = \{Q\} - [B]^T\{\sigma_j\}A \tag{A20}$$

where $\{Q\}$ is the applied load vector for the triangle, $\{\sigma_j\}$ is the stress deviation in the element calculated using the current velocities, and A is the area of the triangle. The matrix $[D_t]$ relates $d\epsilon_{ij}$ to dS_{ij} according to (7b) and at the current velocities.

Equation (A20) indicates that each iteration can be regarded as a linear problem. We assume that the initial estimate in the Newton process satisfies the complete boundary conditions for region A. This is always possible since parameter tracking [6] is used; i.e. the solution for the linear case, $n = 1$, is employed as initial estimate for $n = 2$, and $n = 2$ solution is employed as initial estimate for $n = 3$ and so on. Thus we have an initial estimate not only for the velocities but also for λ_i $(i = 1, 5)$ and μ_1. For each iteration, the increments in the velocities satisfy the incompressibility constraints and the homogeneous boundary conditions obtained by replacing all constant terms (such as u and v) in the boundary conditions, shown in Fig. 3, by zeroes. The solution for each iteration yields the increments in the velocities and the increments in the forces λ_i and μ_1 which are then added to the current values to update these variables. The process converges rapidly after a few iterations. Application of the special boundary conditions by the above method does not increase the number of iterations necessary for convergence; it increases the computer time per iteration only by a relatively insignificant amount. Once again the reader is reminded that although for definiteness most of the discussions in this appendix were referred to the coarse mesh in Fig. 4(a), they hold for any mesh; only the number of variables is larger for a finer grid. In our computations, we used the mesh shown in Fig. 4(b). The complete nonlinear boundary value problem is now solved.

In (A20) replacing $[D_t]$ by another matrix $[D_s]$ which relates ϵ_{ij} to S_{ij} according to the power law relationship (7b) and at

the current velocities, (A20) becomes the equation for a linear iterative process. A useful discussion of this process and its relation to the Newton-Raphson scheme is given in the Appendix of [19]. Some conditions for the convergence of the Newton's method are given by the Kantorovich theorem[20]. Since the linear iterative process converges under less stringent conditions than the Newton process, with the same initial estimate it is possible that the latter process diverge while the former converge. On the other hand, the rate of convergence is of second order for the Newton's method and only of first order for linear iterations. The most efficient scheme (adopted here) is to perform the first few iterations linearly until the result is sufficiently close to the actual solution and then revert to the Newton-Raphson scheme.

It can be shown that the above method of imposing the boundary conditions and Needleman and Shih's method of incorporating the incompressibility constraints are equivalent to the Lagrange multiplier technique. In the former case, the Lagrange multipliers are the forces λ_i and μ_i defined for the coarse mesh by the equations (A16) and (A17) and the constraints are the boundary conditions (A13). In the latter case, the Lagrange multipliers are the hydrostatic stresses and the constraints are the equations expressing the condition $\epsilon_x + \epsilon_y = 0$ in each element. Since the physical interpretation of the Lagrange multipliers (as nodal forces or as hydrostatic stresses) are known beforehand, we preferred the above direct exposition to one given in terms of Lagrange multipliers.